ADVANCED MATERIALS
www.advmat.de

Photoannealing of Microtissues Creates High-Density Capillary Network Containing Living Matter in a Volumetric-Independent Manner

*Maik Schot, Malin Becker, Carlo Alberto Paggi, Francisca Gomes, Timo Koch, Tarek Gensheimer, Castro Johnbosco, Liebert Parreiras Nogueira, Andries van der Meer, Andreas Carlson, Håvard Haugen, and Jeroen Leijten**

The vascular tree is crucial for the survival and function of large living tissues. Despite breakthroughs in 3D bioprinting to endow engineered tissues with large blood vessels, there is currently no approach to engineer high-density capillary networks into living tissues in a scalable manner. Here, photoannealing of living microtissue (PALM) is presented as a scalable strategy to engineer capillary-rich tissues. Specifically, in-air microfluidics is used to produce living microtissues composed of cell-laden microgels in ultrahigh throughput, which can be photoannealed into a monolithic living matter. Annealed microtissues inherently give rise to an open and interconnected pore network within the resulting living matter. Interestingly, utilizing soft microgels enables microgel deformation, which leads to the uniform formation of capillary-sized pores. Importantly, the ultrahigh throughput nature underlying the microtissue formation uniquely facilitates scalable production of living tissues of clinically relevant sizes (>1 cm^3) with an integrated high-density capillary network. In short, PALM generates monolithic, microporous, modular tissues that meet the previously unsolved need for large engineered tissues containing high-density vascular networks, which is anticipated to advance the fields of engineered organs, regenerative medicine, and drug screening.

1. Introduction

The vascular tree is of essential importance to the survival and function of virtually all living tissues.[1] Yet, traditional tissue engineering approaches typically lack a vascular tree and thus solely rely on diffusion to access and dispose of cell-fate-controlling molecules such as oxygen, nutrients, waste products, and growth factors.[2,3] Diffusion rates effectively and inherently limit the penetration of nutrients and oxygen into these tissues, which places strict limitations on the size of engineered tissues if they are to remain viable.[3,4] In the body, native tissues overcome this limitation by containing high-density capillary networks that homogeneously deliver molecules to and from cells.[5] Engineering high-density capillary networks into engineered tissues thus represents a key stepping stone toward engineering clinically sized tissues.[6] However, despite significant advancements in the biofabrication of tissues

M. Schot, M. Becker, C. A. Paggi, F. Gomes, C. Johnbosco, J. Leijten
Leijten lab
Department of Developmental BioEngineering
TechMed Centre
University of Twente
Enschede 7522AE, The Netherlands
E-mail: jeroen.leijten@utwente.nl

T. Koch, A. Carlson
Department of Mathematics
University of Oslo
Oslo 0316, Norway

T. Gensheimer, A. van der Meer
Department of Applied Stem Cell Technology
TechMed Centre
University of Twente
Enschede 7500AE, The Netherlands

L. P. Nogueira
Oral Research Laboratory
Institute of Clinical Dentistry
University of Oslo
Oslo 0316, Norway

H. Haugen
Department of Biomaterials
Institute of Clinical Dentistry
University of Oslo
Oslo 0316, Norway

The ORCID identification number(s) for the author(s) of this article can be found under https://doi.org/10.1002/adma.202308949

DOI: 10.1002/adma.202308949

containing larger blood vessels as well as plentiful examples of capillary networks generated inside small scale hydrogels,[7–9] a strategy to realize the integration of high density capillary networks into clinically sized engineered tissues has remained elusive.

Numerous techniques have been used to explore the creation of blood vessels, including electrospinning,[10] molding,[11] cellular cocultures,[12] angiogenic biomaterials,[13] two-photon lithography,[14] and bioprinting.[15] Although these biofabrication strategies have proven successful in producing blood vessels that possess a diameter and tissue density resembling native arteries,[16,17] veins,[18,19] arterioles,[20] or venules,[21] the missing piece is the realization of high density 3D capillary networks within living tissues. For example, embedded 3D printing has been widely adopted for its ability to print channel-like structures in true 3D freeform inside a supporting phase that can be solidified to form engineered tissue containing hollow channels.[22–25] Although this can endow hydrogel constructs with a few channels that together form a 3D branched network, these channels are typically characterized by diameters upward of 100 μm, corresponding to arterioles and arteries that supply nutrient carrying blood to tissues.[26] However, the capillaries that deliver blood to the cells to omit the otherwise large diffusion distances are ≈5–40 μm in diameter[1] and require a drastically higher density to function (e.g., on average 6×10^8 capillaries per cm^3 of tissue in the human body).[27] Consequently, the inherent trade-offs between speed and resolution for all current biofabrication approaches have rendered the engineering of high-density capillary networks into living tissues an unresolved challenge.

Inspired by the annealing of inanimate microgels into microporous annealed particle scaffolds that have been explored for among others, wound healing,[28–30] delivery of drugs,[31] and stem cells,[32] we hypothesized that the annealing of living microtissues could be leveraged to create large engineered living tissues that contain a high-density capillary network. Specifically, a packed bed of spheres inevitably contains an inherent, high-density network of interconnected pores, of which the pore space dimensions can be controlled via the packing density, monodispersity, and size of the spherical building blocks. Although there exists an extensive body of microannealed particle (MAP) scaffolds within literature, the harsh cross-linking conditions (pH,[28] nonphysiological temperatures,[32] UV irradiation,[33–35] mechanical force)[36] utilized to generate microgels or to anneal microgels into porous scaffolds limit their compatibility for fabricating living, modular, tissues containing a (pre)vascularizable capillary blueprint. Specifically, the ability of initially lifeless MAP scaffolds to become living tissues is dependent on postfabrication cell seeding, cellular migration from an adjacent tissue, and/or angiogenesis from adjacent blood vessels. While it is possible to design a MAP that allows for cells to eventually enter the annealed microgels themselves, the migrating cells will initially enter the construct via the pore spaces between annealed microgels, which effectively clogs-up the preexisting microporosity. This limits hydraulic conductivity, hinders diffusion of nutrients, demands the presence of an external cell source, and requires substantial amounts of time for the scaffold to develop into a living tissue. To address this, we reasoned that the features of packed spheres could be leveraged and combined with annealable living building blocks to directly create a living tissue containing an interconnected hollow microporosity with a capillary-sized diameter.[37,38] In this manner, we envisioned to engineer modular living porous tissues that not only support cellular ingrowth within the minor volume represented by the porous space, as seen in conventional MAP scaffolds, but already immediately contain cells within the bulk of the tissue, namely inside the microgels, in a cell-migration-independent manner (**Figure 1a**).

In this study, we showcase photoannealing of living microtissue (PALM) as a novel biofabrication method to produce engineered tissues of clinically scalable volumes containing inherent high-density capillary-like networks. This was achieved via the ultrahigh throughput production and photoannealing of living microtissues, composed of cells and soft alginate–tyramine (ATA) microgels, using in-air microfluidics.[39] Annealing occurred via cytocompatible visible light cross-linking of tyramine moieties, which formed large monolithic living tissues with an interconnected network of capillary-sized pores that could be vascularized. The capillary-like network facilitated near-instantaneous and homogenous delivery of small molecules (i.e., nutrients and oxygen) with a maximal diffusive length of 75 μm throughout the entire tissue volume, which uniquely was independent of the size of the engineered tissue owing to the diffusive distance being determined by the size of the original microtissues. In short, we present a bottom-up tissue engineering solution that overcomes the trade-off between resolution and speed posed by traditional biofabrication methods, enabling straightforward engineering of large living tissues containing a high-density capillary network.

2. Results and Discussion

2.1. Production of Clinically Relevant-Sized Engineered Tissues via Ultrahigh Throughput Production of Microgels Using In-Air Microfluidics and PALM

To allow for the production of large tissues composed of living microtissues, we explored ultrahigh throughput production of cell-laden microgels using in-air microfluidics, which is a chip-free and oil-free microfluidic approach (Figure 1a). A jet containing a 0.5% w/v alginate solution was piezoelectrically actuated to generate a monodisperse droplet train (Figure 1b and Figure S1 and Video S1 (Supporting Information)). Alginate was selected as the base material due to its compatibility with in-air microfluidics, which necessitates a rapid (subsecond) cross-linking.[39–41] This droplet train collided with a second liquid jet containing calcium chloride, which effectively wraps around each droplet via surface tension-driven Marangoni flow, and subsequently ionically cross-linked the alginate in the droplet to form a microgel. To ensure homogenous cross-linking of the alginate droplets, the surface tension of the second jet was lowered by the addition of a small amount of ethanol (10% v/v) to match the rapid ionic cross-linking during the ≈100 ms flight time before droplet collection. Using this approach, alginate microgels were produced in an ultrahigh throughput manner that was >300 times faster than conventional chip-based microfluidic droplet generation approaches. For example, monodisperse cell-laden microgels with an ≈75 μm radius could be produced at a throughput of up to 150 mL h^{-1} (Figure 1c).[42] Furthermore, it was also demonstrated that microgels of varying sizes could be generated by changing the

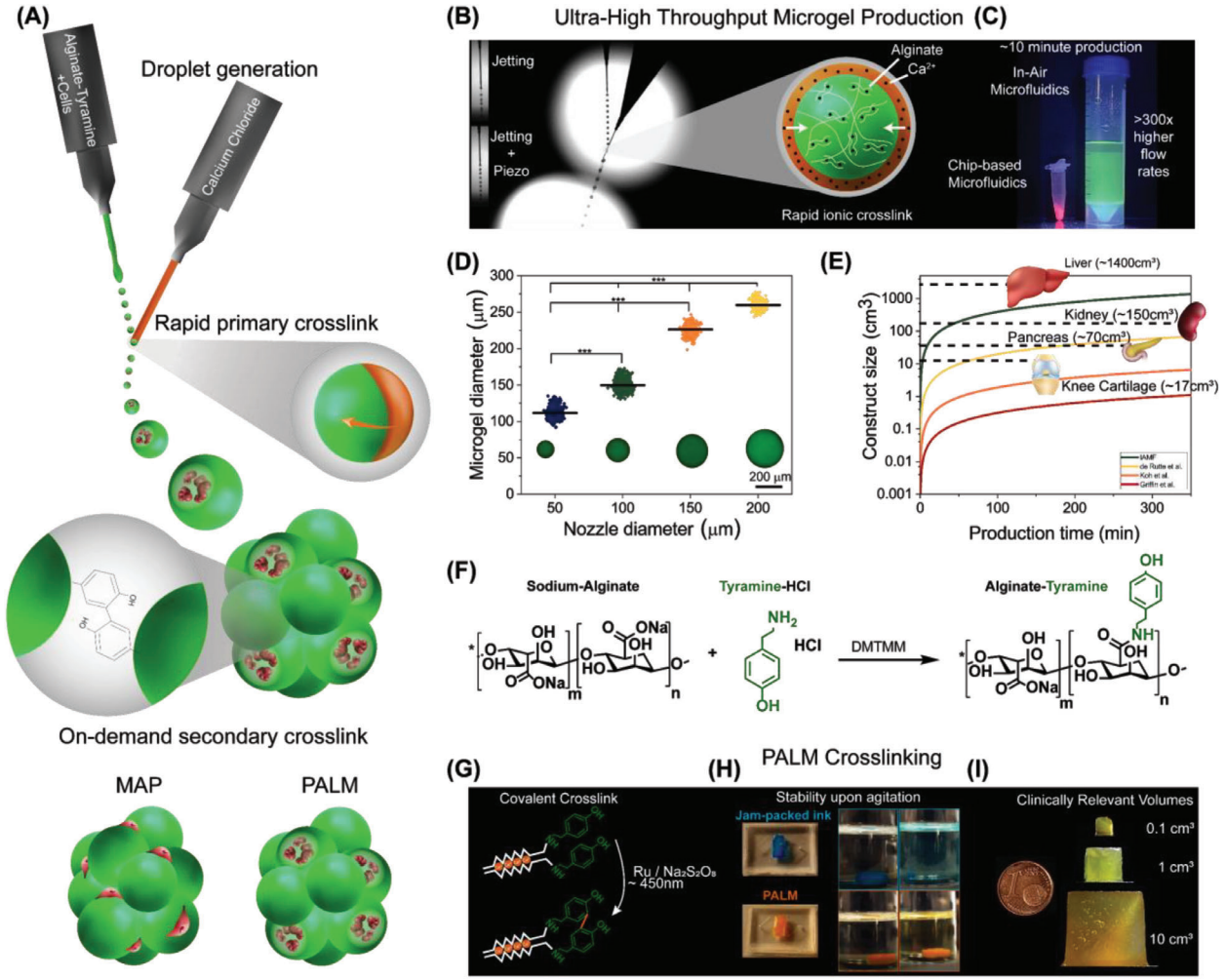

Figure 1. In-air microfluidics enabled ultrahigh throughput production of two-step cross-linkable microgels for the formation of clinically relevant sized PALM-generated tissues. a) Schematic depiction of the process of creating microgels and engineered tissues through PALM and schematic depiction of the difference between conventional MAPs and PALM. b) A stable droplet train is produced by applying piezoactuation to a liquid alginate jet. Upon collision with a $CaCl_2$ jet, microgels are formed through physical cross-links. c) This droplet formation approach results in a >300-fold increase in production throughput compared to conventional chip-based microfluidics. d) Microgel sizes produced using in-air microfluidics with varying nozzle sizes. $N > 300$, line indicates mean, significance $p < 0.001$ is indicated by *** (one-way ANOVA with Tukey's post hoc test). e) Production speed of in-air microfluidics compared to currently available production methods for microgels used as building blocks for PALM. The y-axis here represents the amount of microgels needed to engineer a tissue of a certain volume using PALM assuming a random dense packing of microtissues (i.e., ≈63% of the volume). f) Reaction scheme for the functionalization of tyramine (TA) onto sodium alginate using DMTMM chemistry to enable dual-cross-linkable ATA microgels. g) ATA can be covalently cross-linked using the radical reaction of ruthenium, sodium persulfate, and visible light. This reaction is used to anneal ATA microgels through PALM. h) Upon hydrodynamic agitation, jam-packed inks redisperse rapidly, whereas PALM-engineered constructs maintain their integrity. i) Due to the ultrahigh throughput production speeds of in-air microfluidics and the dual-cross-linkable material, PALM enabled the generation of clinically relevant sized (shown up to 10 cm^3) constructs (on the order of minutes).

nozzle diameters of both the primary and secondary jets (Figure 1d). Plotting the produced volume as a random dense packed construct (i.e., 64% of the volume is occupied by spheres) against production times revealed that this approach allows for the production of sufficient quantities of microgels to form clinically sized living implants in a period of time that is compatible with intraoperation procedures (Figure 1e). Importantly, in-air microfluidics has a per-nozzle throughput that is 20 times higher than extensively parallelized chip-based microfluidic systems used to produce annealable microgels that are reported in literature,[28] enabling the production of >10 cm^3 constructs in mere minutes. Taken together with the clean (e.g., oil-free and surfactant-free) nature of the approach, this makes in-air microfluidics a uniquely suitable technology platform for the production of clinically translatable microporous living tissues.

To enable the photoannealing of microgels into a microporous yet monolithic large construct, we functionalized tyramine groups onto the alginate backbone through 4-(4,6-dimethoxy-1,3,5-triazin-2-yl)-4-methylmorpholinium chloride (DMTMM) chemistry to synthesize ATA. The degree of substitution could be controlled during synthesis by changing the amount of DMTMM

and tyramine added in the process (Figure 1f and Figure S2 (Supporting Information)), and ATA with a degree of substitution of ≈4.2% used for all experiments. Tyramine-modified alginate formed microgels in a similar fashion as pristine alginate using in-air microfluidic microgel production with the same flow parameters, as polymer solution viscosity and the ionic cross-linking rate remained virtually identical. Subsequently, ATA microgels were packed through injection molding, spiked with ruthenium and sodium persulfate via diffusion, and photoannealed in situ via covalent tyramine coupling using visible light (Figure 1g). The resulting microporous hydrogels possessed storage moduli of ≈4 kPa (Figure S3, Supporting Information) and were demonstrated to be mechanically stable under hydrodynamic agitation, while non-cross-linked jam-packed microgels readily dispersed when exposed to identical agitation (Figure 1h). This modular assembly approach enabled the production of stable constructs of >10 cm^3 (Figure 1i).Together, this demonstrated that in-air microfluidics enables the ultrahigh throughput production of dual-cross-linkable ATA microgels which, upon photoannealing, allowed for the generation of clinically relevant sized constructs at an unprecedented rate.

2.2. Photoannealing of Soft Microgels Creates Capillary-Sized Porous Spaces in a Microgel-Size-Independent Manner

To analyze the internal 3D interconnected channel structures of the engineered constructs, X-ray microcomputed tomography (micro-CT) was used to 3D image and visualize the void space in high resolution. This analysis confirmed our hypothesis that PALM forms highly interconnected internal pore space networks (**Figure 2a**). Quantification of the 3D network revealed that each pore was directly connected to 4.2 ± 2.5 other pores on average (Figure 2b and Video S2 (Supporting Information)). Moreover, 3D-reconstructed micro-CT images suggested that the originally perfectly round microgels became slightly deformed prior to being photoannealed into an engineered microporous construct. We reasoned that this deformation could be explained by the softness of the used microgels which, therefore, could potentially be used to control the internal architecture of the interconnected internal pore network.

To investigate the effect of the annealable microparticles on the pore network's architecture, we visualized and compared the internal pore networks of constructs that were formed using annealed soft ATA microgels and random close-packed hard polystyrene (PS) microspheres. Although both types of microparticles were of near-identical size, they varied notably in terms of equivalent pore diameter within packed beds (Figure 2c). Importantly, the microparticles significantly differed in terms of Young's modulus, which was determined to be 15 ± 2.0 kPa for ATA microgels and ≈3.0 GPa for polystyrene microparticles (Figure 2d and Figure S3 (Supporting Information)). This difference in microparticle stiffness was indeed revealed to correlate with shape stability as the stiff microparticles maintained their perfectly round shape upon packing, while the softer microparticles consistently deformed (Figure 2e).

The packed soft spheres appear to deform into an almost hexagonal form (Figure 2e), reminiscent of structures also found in foams created by capillary force.[43,44] We believe capillary forces, generated directly prior to annealing, are also important in our system, leading to narrower pores in all annealed microgel constructs when using soft microgel spheres. As interstitial solvent is drained from below the microgels, a liquid meniscus forms between the soft spheres, creating a capillary pressure that pulls them closer together. The capillary pressure scales with the surface tension coefficient between the solvent and the air, $\gamma \approx 73$ mN m^{-1}, and the meniscus formed between the spheres that is expected to have a radius close to the sphere radius, $R = 75$ µm, when closely packed. Elastic deformation u_z in the sphere is resisting the capillary suction pressure, which relates directly to the material's Youngs modulus $E \approx 15 \pm 2.0$ kPa. Then, by balancing the pressure from capillary suction $P_\gamma \sim \gamma/R$ with the elastic stress $P_E \sim Eu_z/R$, we get a length scale for the deformation $u_z \sim \gamma/E$, also known as the elastocapillary length. Inserting the material parameters gives a deformation length of the spheres $u_z \sim \gamma/E \approx 5$ µm, an order of magnitude similar to experimental observations (Figure 2e). When the size of the spheres becomes comparable to u_z, additional elastic effects need to be accounted for to predict the deformation.

This deformation was demonstrated to offer an advantageous effect in terms of microparticle packing. While stiff microparticles followed standard packing theory by demonstrating a void fraction corresponding with the random close packing limit[45] (≈36%), soft microparticles were characterized by a void fraction that was lower than the absolute theoretical limit set for close packing of solid spheres (<26%)[46] (Figure 2f). This confirmed that microparticle stiffness can thus be leveraged to control the architecture of the pore network via microparticle deformation.

To further elucidate what functional effects microparticle deformability has on the internal pore architecture, we compared microparticles of different sizes and stiffnesses. For rigid nondeforming microparticles, the pore diameters within packed beds positively correlated with microparticle size as dictated by packing theory (Figure 2g).[47,48] However, when comparing soft and hard microparticles of similar size, the pores were drastically smaller (i.e., smaller peak and average pore diameters) for the softer microparticles (Figure 2h). This observation corresponds with the previous phenomenon of microgel deformation, leading to reductions in both void fraction and pore diameters. Interestingly, unlike for the case of stiff microparticles, the effect of microgel size on the equivalent pore diameter distributions was negligibly small for soft deformable microparticles (Figure 2i). In fact, regardless of the radius of the microgel sample used, the largest fraction of pores within the engineered microporous constructs contained diameters matching that of capillaries (<40 µm). The dynamic process involved in the formation of pores is an interesting avenue for future in-depth analysis, where the variations in material cross-linking (and potential gradients), capillary forces and elastic relaxation of the deformed spheres, and the motion of the interstitial fluid are likely to play a role in the pore size distribution.

To determine the functional resemblance between engineered capillary networks and natural microcapillary networks, we demonstrated that the predicted hydrodynamic wall shear stress (WSS) distribution experienced by the internal micropore network of our engineered constructs resembled that of the forces experienced in a native murine microvascular network

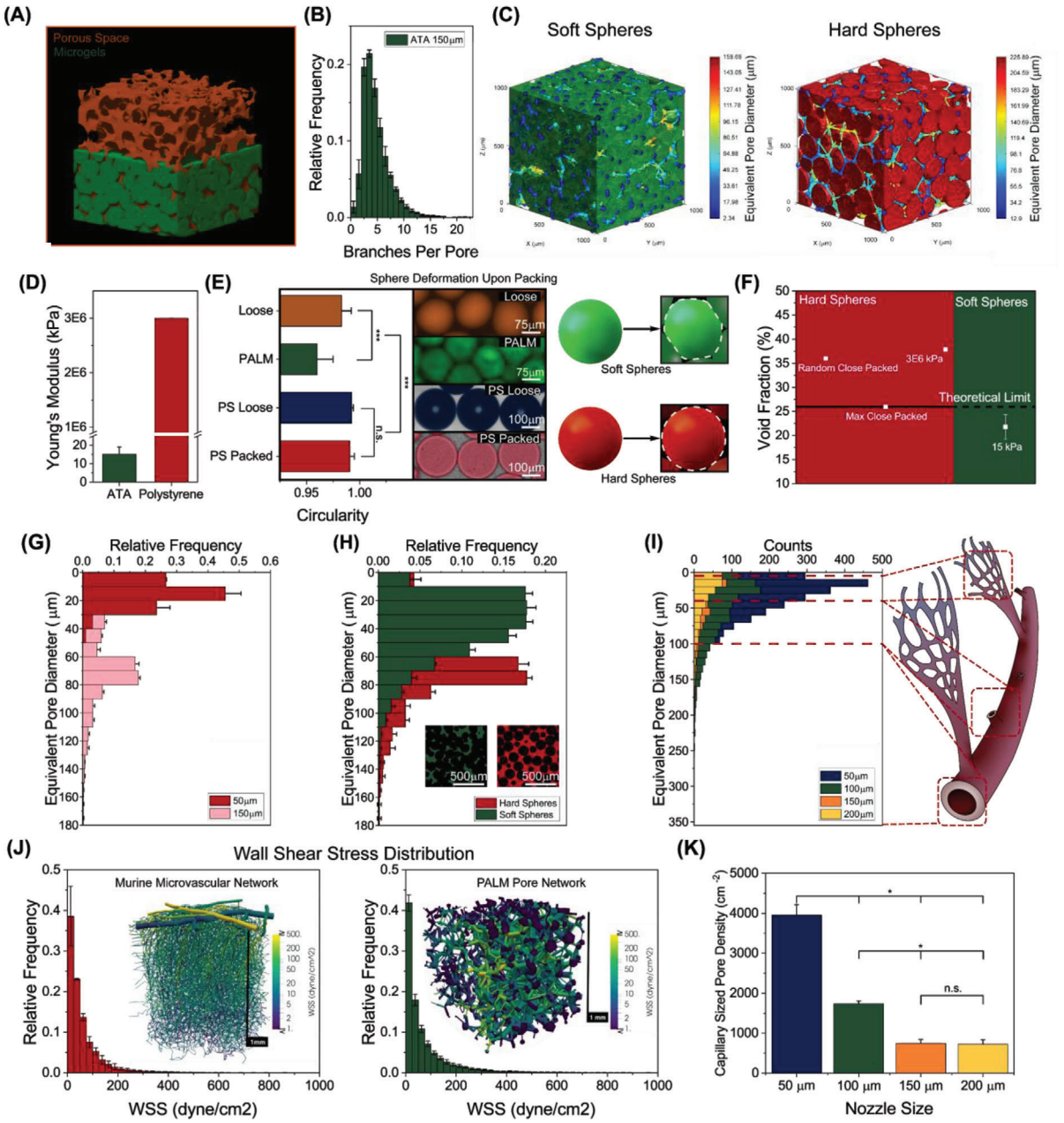

Figure 2. Soft microgel building blocks enable PALM with inherent capillary-sized pore networks. a) 3D rendered visualization of PALM-generated constructs with microgels in green and void space in orange. b) Interconnectivity of the void space in ATA PALM-generated constructs, indicated by the amounts of branches per pore node (≈4 branches per node on average), $n = 3$. Error bars indicate standard deviation. c) 3D pore networks generated using MATLAB programming to quantify the pore networks generated through PALM and packed polystyrene spheres. d) Comparison of the stiffness of ATA microgels ($n = 30$) and polystyrene spheres, showing a difference of six orders of magnitude. Error bars indicate standard deviation. e) Circularity changes measured in ATA gels and PS spheres upon PALM and packing, respectively, $n = 30$. Error bars indicate standard deviation, significance of $p < 0.001$ is indicated by ***, n.s. indicates no significant difference (one-way ANOVA with Tukey's post hoc test). f) Void fraction of packed polystyrene (3×10^6 kPa) and PALM-generated ATA constructs (15 kPa) compared to theoretical values of random dense packed (≈35% void space) and the maximum packing density (≈25% void space). g) Pore size distribution for 50 and 150 μm packed PS spheres showing a shift of the pore size distribution to larger diameters when larger spheres are used ($n = 3$). Error bars indicate standard deviation. h) Pore size distribution for soft ATA PALM-generated constructs compared to hard packed PS beds of the same sized spheres. Insets show a single slice as generated using micro-CT for both soft (green) and hard (red) spheres ($n = 3$). Error bars indicate standard deviation. i) Pore size distributions of PALM-generated constructs made of soft ATA of varying sizes ($n = 3$). Red dashed lines are superimposed to denote the size of capillaries (<40 μm), arterioles (40–100 μm), and arteries (>100 μm). j) Wall shear stress distributions generated with flow simulations in mouse vascular networks ($n = 2$) and PALM-generated constructs. Error bars indicate standard deviation. k) Capillary-sized pore density as a function of the nozzle size used to generate the microgel building blocks for PALM ($n = 3$). Error bars indicate standard deviation, significance of $p < 0.05$ is indicated by *, n.s. indicates no significant difference (one-way ANOVA with Tukey's post hoc test).

(Figure 2j). Our computational results showed that the WSS distributions are not sensitive with respect to the nonlinear diameter-dependent resistance changes caused by the presence of red blood cells (RBCs, stabilize flow).[49,50] Absolute WSS levels (and the mean flow velocity) in the engineered capillary networks can be tuned during liquid perfusion by adjusting the driving force. Since the microgel pore structure matched typical blood capillary diameters, upon vascularization of the pore space, endothelial cells can thus be subjected to physiologically relevant levels of shear stress.[51,52] Finally, we revealed that changing the microgel size directly controls the total amount of capillary-like pores within the engineered constructs (Figure 2k). This feat thus offers the possibility to engineer (living) constructs with controlled capillary density without altering capillary diameter in a facile, straightforward, and scalable manner.

2.3. PALM Enables the Engineering of Living Tissues Containing a High-Density Vascularizable Capillary-Sized Pore Network

While some pioneering studies have explored the annealing of inanimate microgels into microporous annealed particle scaffolds, we hypothesized that this strategy could also be explored for the annealing of living microtissues. Based on our observations, we reasoned that annealed living microtissues would also inherently contain a capillary-like pore network, which represents an innovative method to engineer living tissues with integrated capillary networks (**Figure 3a**) at scale. To achieve this, we produced annealable living microtissues composed of hepatocytes within ATA microgels, which were produced using in-air microfluidics. By tuning the cell concentration in the ATA polymer solution, the number of cells within the engineered microtissues can be accurately controlled, resulting in 7 ± 2, 15 ± 4, 30 ± 5, 39 ± 9, and 56 ± 9 cells per microgel when using concentrations of 1×10^6, 3×10^6, 5×10^6, 7×10^6, and 10^7 cells mL^{-1}, respectively (Figure 3b,c). Importantly, although ethanol is initially used to facilitate the homogenous in-air cross-linking of the microgels, ethanol does not pose severe cytotoxicity to cells due to the short in-flight contact time with ethanol (≈100 ms) before it is diluted in an excess of culture medium to a concentration of ≥1% which has been reported as nontoxic for exposure times below 24 h.[41] As a result, both the ionic cross-link used for microgel formation, and the visible-light-initiated radical reaction used for PALM are associated with a low cytotoxicity as evidenced by high cell viability (e.g., >80%) (Figure 3d,e). Importantly, using culture medium as the solvent did not negatively affect the photoannealing process (Figure S5, Supporting Information). The ability of PALM to maintain viability and structural cell organization over time was visualized based on phalloidin/4′,6-diamidino-2-phenylindole (DAPI)-stained PALM-generated tissues that were cultured for seven days (Figure 3f and Video S3 (Supporting Information)).

We next reasoned that the capillary-like pore spaces between the annealed living microtissues could act as highways for vascularization resulting in endothelialized capillary networks (Figure 3g). To demonstrate this ability, a collagen I solution containing human umbilical vein endothelial cells (HUVECs) was introduced in the capillary-like pore spaces between the living microtissues and cultured in the presence of vascular endothelial growth factor for a period of seven days. Fluorescent staining of vascular endothelial cadherin (VE-Cadherin) was used to visualize the formed vascular networks. Confocal microscopy revealed intricate networks of endothelial cells that had self-assembled into smaller and larger vessels (Figure 3h). Moreover, orthogonal views confirmed the presence of lumens within the formed capillaries (Figure 3i). Indeed, the visual colocalization of lumens and microgels confirmed that vessels formed in the capillary-like pore spaces between microgels, where endothelial cells were directly proximal to the microgel and formed open lumens in the interstices (Figure 3j). Although collagen I was used to facilitate cell growth into the capillary-like space between the microgels, microgel building blocks could also be functionalized or preseeded with endothelial cells to enable vascularization of PALM-generated tissues.[53,54]

To demonstrate that the capillary networks between the annealed living microtissues were fully functional, we investigated their ability to be perfused with RBCs, which is a key function of native capillary networks of our blood circulatory system (Figure 3k). To this end, we covalently annealed our microgels within a microfluidic device (Figure S6, Supporting Information), which represents an effective strategy to endow organ-on-chip models with an integrated capillary network. Subsequently, RBCs were circulated through the capillaries of the on-chip engineered tissue construct. This confirmed that high concentrations of RBCs were readily able to pass through the capillary-like pore network (Figure 3l and Video S4 (Supporting Information)). Moreover, time-resolved microscopic tracking of individual RBCs revealed that distinct RBCs could move through the constructs via different flow paths, which emulates the natural behavior of capillary networks of native tissues (Figure 3m). Finally, confocal microscopic analysis of fluorescently labeled RBCs demonstrated that the geometry of the engineered capillary network also emulated another naturally occurring feature of native capillaries, which was the squeezing of RBCs to facilitate their passing through the capillary network (Figure 3n). In short, we demonstrated the engineering of viable, cell-dense tissues through PALM, which allowed for rapid vascularization and formation of capillaries within their pore space. As the fabrication of the prevascularized PALM-generated tissues is highly scalable, they address the previously unmet need of creating viable large engineered tissues within the field of regenerative medicine. Conversely, PALM was demonstrated to allow for miniaturization to offer high density vascularity and minimization of diffusive lengths within microfluidic devices to generate highly modular vascularized organ-on-chips.

2.4. High Density Capillary Networks Generated through PALM Enable Near-Instant and Homogenous Delivery of Nutrients and Oxygen throughout Large Engineered Tissues

Tissue engineering has traditionally been constrained to relatively small engineered constructs due to the limited diffusion of oxygen and nutrients into large tissues.[6] However, the capillary-like pores within PALM-generated constructs allow for a drastically improved hydraulic conductivity, thus offering near-free flow of liquids (such as blood) (**Figure 4a**). The highly perfusable nature of the integrated capillary bed within

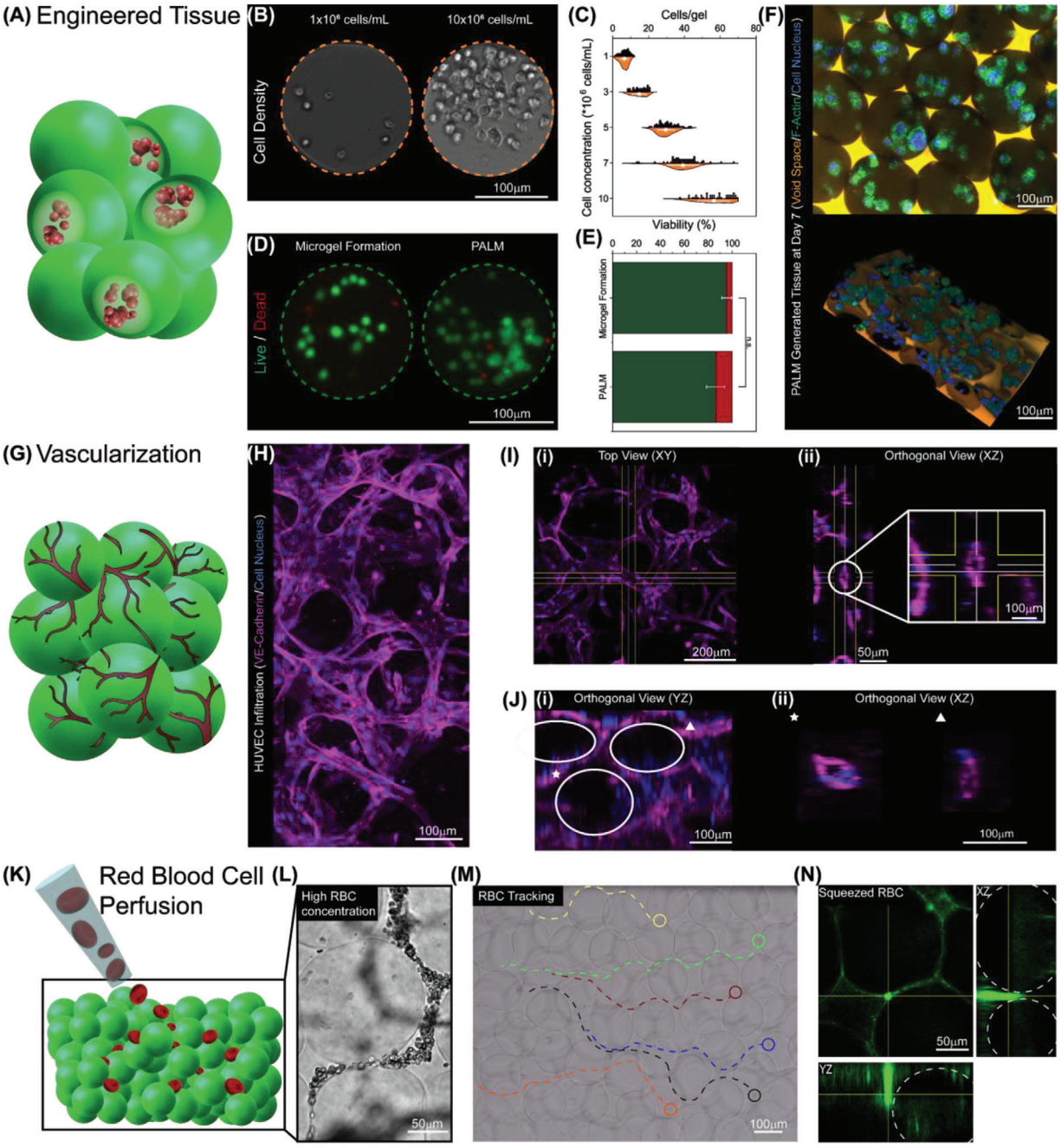

Figure 3. Engineered and vascularized tissues generated through PALM. a) Schematic depiction of microgels containing cells annealed into a monolithic tissue through PALM. b) Microphotograph of microgels containing distinct concentrations of hepatocytes. c) Quantification of the amount of encapsulated cells per microgel dependent on the cell concentration in the precursor solution ($n > 35$). d) Fluorescence microscopy image of cell viability after encapsulation (i.e., physical cross-link) and PALM (i.e., covalent cross-link). e) Quantification of cell viability postencapsulation and post-PALM ($n = 3$, >400 cells per sample). Error bars indicate standard deviation, n.s. indicates no significant difference (one-way ANOVA with Tukey's post hoc). f) Fluorescence confocal microscopy image and 3D reconstruction of an engineered tissue generated through PALM using living building blocks after seven days of culture. Cells and interstitial space are fluorescently labeled with Phalloidin/DAPI and Tetramethylrhodamine-Dextran (TRITC–Dextran), respectively. g) Schematic depiction of PALM-generated construct's ability for vascularization of the capillary pore space. h) Confocal maximum intensity projection of VE-Cadherin/DAPI-labeled HUVECs growing into the void space within packed microgels. i) i) Top view of a confocal slice (same fluorescent labeling as (f)) including ii) an *XZ* orthogonal view showing an open capillary-sized vessel including zoom-in. j) i) Orthogonal view of the confocal *Z*-stack with spheres superimposed and ii) zoom-ins revealing open vessels. k) Schematic depiction of an interconnected capillary network engineered through PALM that allows for red blood cell perfusion. l) Microscopy image showing RBC perfusion within the capillary pore spaces of a PALM-generated construct. m) Microscopic image particle tracking of diluted RBCs being perfused through a PALM-generated construct over a period of 2 s. Each colored line represents a different red blood cell. n) Fluorescent confocal slice including orthogonal views of a $DiOC_6$-labeled RBC squeezing through the capillary space within a PALM-generated construct.

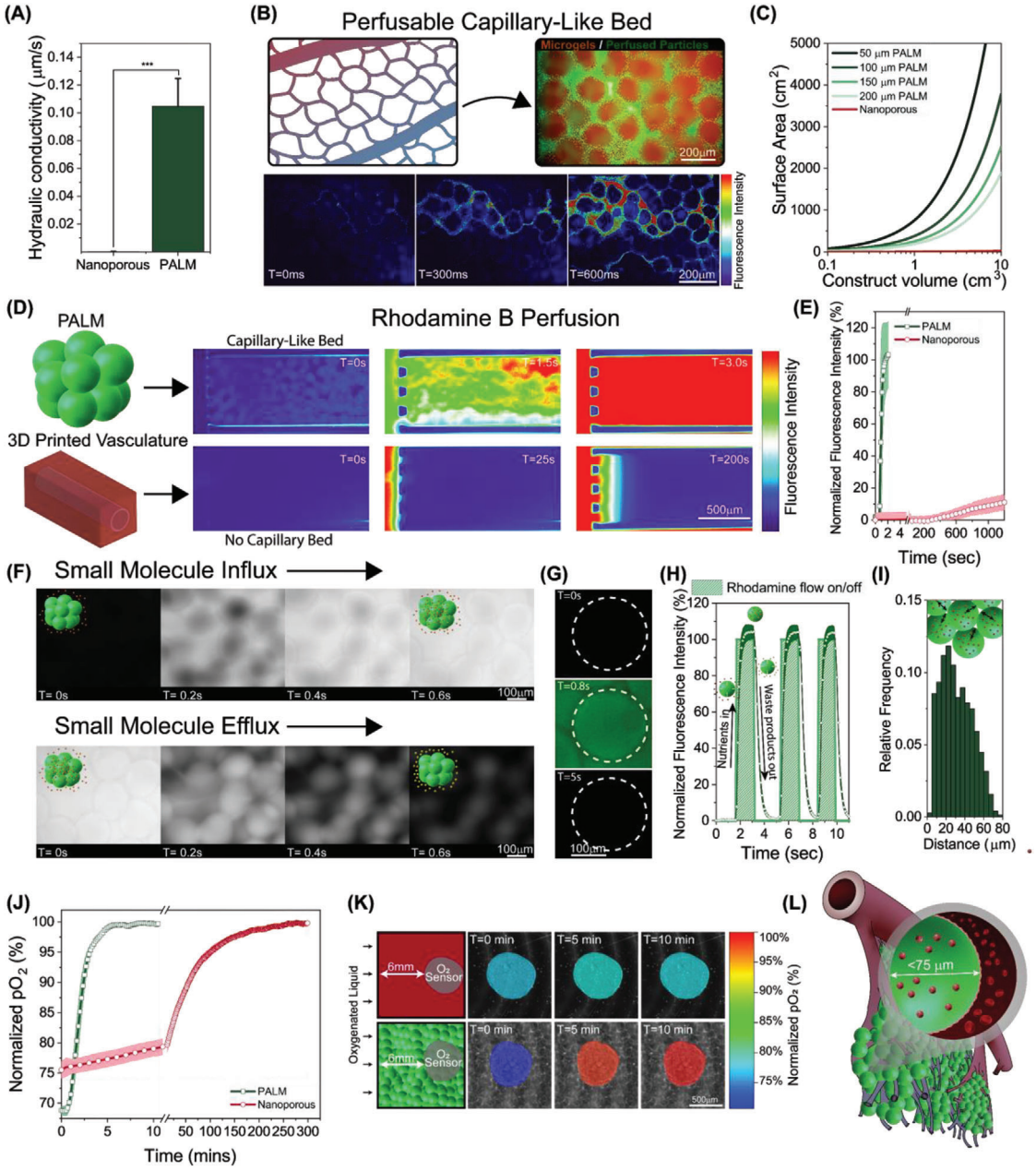

Figure 4. PALM-dictated architecture enables minimization of diffusive distances in engineered tissues. a) Hydraulic conductivity of ATA PALM-generated constructs as compared to nanoporous alginate hydrogels ($n = 3$). Error bars indicate standard deviation, significance of $p < 0.001$ is indicated by *** (one-way ANOVA with Tukey's post hoc test). b) Schematic depiction of a capillary bed and a microscopy image of a PALM of which the pore space was filled with fluorescent micrometer sized beads. The bottom panel shows the infusion of fluorescent micrometer sized beads into a capillary pore network engineered through PALM. c) Calculated surface area of tissues engineered through PALM using a variety of building block sizes as well as of a nanoporous hydrogel construct (calculated as a square). d) Comparison of nutrient infusion into PALM-generated and hydrogel constructs analog to 3D printed vessels (i.e., large vessel with nanoporous hydrogel next to it). e) Quantification of the fluorescent intensity of rhodamine B at 2 mm depth within the PALM-generated constructs and nanoporous hydrogels in a time-resolved manner ($n = 3$). f) Confocal fluorescence microscopy images of the influx and efflux of small molecules (i.e., rhodamine B) between the microgel building blocks and capillary pore spaces of PALM-generated constructs showing a homogeneous and near-instant response of all microgels. g) Confocal fluorescence microscopy images of rhodamine B (colored in green) influx and efflux within a single microgel annealed through PALM and its adjacent pore space. h) Quantification of the time it takes for small molecules (i.e., rhodamine B) to diffuse in and out of microgels annealed through PALM ($n = 3$). i) Distribution of the distance of individual cells within microgels to the nearest pore ($n > 500$ cells, 30 microgels). j) Quantification of partial oxygen pressure levels within a degassed PALM-generated construct and a degassed nanoporous hydrogel construct upon influx of an oxygen carrying liquid ($n = 3$). k) Visualization of (j), colored spots indicate the oxygen sensors at 6 mm depth into the construct with the normalized oxygen partial pressure superimposed as a color. l) Schematic depiction of PALM's ability to form tissues with high density capillary networks while allowing for homogeneous and near-instant local nutrient, and oxygen exchange in a construct-size-independent manner.

PALM-generated constructs was visualized within a microfluidic chamber that allowed for the perfusion of the capillary network using micrometer-sized microparticles driven by pressure-controlled pumps (Figure 4b and Video S5 (Supporting Information)). Importantly, the integrated capillary network offers benefits in terms of maximal diffusive lengths by dramatically increasing the construct's surface area in relation to its volume (Figure 4c). By contrast, traditional bulk nanoporous hydrogels barely increase their surface area when scaled to clinically relevant sizes. In other words, in nanoporous hydrogels, the diffusion limit severely affects the cells in the core of the construct as increased size means increased diffusive lengths, while using PALM, the integrated capillary network ensures that the maximum diffusion distance for nutrients, oxygen, and waste products within engineered tissues remains constant as it is dictated not by construct size but by the radius of the individual living microtissue building blocks.

To comparatively study the effect of the reduced maximal diffusive length enabled by the integrated capillary networks, we compared the diffusive rates within PALM-generated constructs to a nanoporous hydrogel of the same biomaterial. Both constructs were supplied with fluids in a microfluidic chip through an inlet channel, which was the engineered analog of an arteriole based on its size and flow speed. To study the distribution rates of nutrients and small molecules, rhodamine B was used as a fluorescent model molecule owing to its size of 479 Da, which is similar to metabolites and small molecules (e.g., most nutrients range between 50 and 1500 Da). Traditional engineered tissues containing large blood vessels are associated with long diffusive lengths, resulting in highly spatially distinct nutrient availability which fluctuates over many minutes to several hours (Figure 4d). In stark contrast, the architecture of our PALM-generated construct reduced the maximum diffusion distance to 75 µm, the radius of its building blocks, which is associated with full and near-instant homogenous distribution of rhodamine B through the entire volume of the engineered construct, as represented by the fluorescence intensity in the images. Time-resolved quantification of the fluorescent signal at a 2 mm distance from the inlet channel of PALM-generated or nanoporous tissues was performed, which highlighted the vast difference in the ability to facilitate the exchange of molecules between PALM-generated tissue and perfusate (e.g., blood) (Figure 4e). To visualize that this drastic difference was indeed caused by the minimal diffusive length (e.g., <75 µm) as programmed by the size of the individual microtissues, high-resolution fluorescence microscopy was performed on PALM-generated tissues that were alternatingly perfused with either rhodamine B or nonfluorescent aqueous solutions. This analysis confirmed that liquids can freely penetrate the capillary-like pores within the PALM-generated tissues via convective flow, and the small molecules transported with the perfusing liquid can subsequently readily diffuse in and out of individual microgels, all within a period of under 3 s (Figure 4f–h and Video S6 (Supporting Information)). Moreover, quantifying the distance from cells within the PALM-generated tissues to the nearest capillary confirmed that the maximal diffusive length within the engineered tissue was indeed reduced to a maximum of 75 µm (Figure 4i). Together, this demonstrates that small molecules (e.g., nutrients and waste products) can be near-instantly exchanged between the engineered circulatory system and all cells within each living microtissue throughout the entire tissue construct in a volumetric-independent manner, which suggests that it could potentially overcome the typical size-induced limitation that hinders the upscaling traditional engineered tissues.[55,56]

We next demonstrated that the rapid diffusion of molecules as mediated by the capillary network in combination with the minimal diffusive distance of the microtissues could functionally improve engineered tissues by, for example, accelerating the supply of oxygen throughout the volume of the engineered tissue. To this end, PALM-generated tissues and nanoporous alginate hydrogels were separately incorporated within oxygen-impermeable microfluidic devices that also contained an optical oxygen sensor, which was positioned at 6 mm distance from the inlet channel. Upon degassing and subsequent perfusion with an oxygenated liquid, similar to the fluorescent small molecules, the partial oxygen pressure level within all annealed living microtissues rapidly equalized to the perfusate (e.g., saturation within 5 min) (Figure 4j). By contrast, the use of a traditional nanoporous alginate gel associated with a drastically slower influx rate of oxygen, which only reached a plateau after ≈5 h (Figure 4k). In particular, this demonstrates that the integrated capillary network of the annealed microtissues promotes the dissipation of unwanted biological gradients by offering rapid exchange rates, reducing undesired spatially and temporally distinct cellular behavior.

Taken together, the photoannealing of soft living microtissues can overcome the key limitation of diffusion limits, which has long hindered the upscaling of traditional tissue engineering approaches. Indeed, engineering blood vessels using biofabrication techniques such as 3D bioprinting can bring blood to and through engineered tissues. However, these approaches typically lack the required high density and interconnected nature that defines the capillary beds that are essential for proper tissue function. Consequently, tissues engineered through traditional approaches are inherently limited in their performance and function due to their inevitably long diffusive lengths. By contrast, the (photo)annealing of living microtissues offers the advantage of integrated engineered capillary-like networks that naturally allow for rapid and homogeneous distribution of nutrients and oxygen throughout the entire volume of the engineered tissue. Moreover, this approach uniquely achieves this by dictating its maximal diffusive lengths based on the individual microtissues size, which thus uncouples the diffusive length from the total construct size. Therefore, this represents a novel approach to a universal engineered tissue design with volumetric diffusive access to nutrients, oxygen, waste products, and growth factors in a scalable yet size-independent manner (Figure 4l).

3. Conclusion

Our results reveal the potential of (photo)annealing of living microtissues to engineer living, monolithic yet microporous tissues containing an interconnected, high-density capillary-like network that serves as a blueprint for vascularization and perfusion. Despite the intricate design of high-density capillary networks within the engineered tissues, these perfusable networks were created within minutes in a simple one-step approach, overcoming the compromise between resolution and speed inherent

to traditional biofabrication approaches such as 3D bioprinting. This novel bottom-up tissue engineering approach effectively uncouples diffusive lengths from construct size by having its maximal diffusive length dictated by the size of the individual microtissues, which in turn enables the creation of viable, large, engineered tissues. The capillary network facilitates near instantaneous and homogeneous delivery of key molecules such as nutrients and oxygen within engineered tissues, circumventing undesired diffusion gradients associated with traditionally engineered tissues. We envision that this novel biofabrication method may find widespread applications ranging from the scalable production of engineered donor organs and advanced drug testing models to lab-grown meat.

4. Experimental Section

Materials: Calcium chloride dihydrate, fluorescein isothiocyanate dextran (FITC-Dex) (2000 kDa), rhodamine B, D−(+)-gluconic acid δ-lactone, calcium carbonate, sodium chloride, lead(II) acetate trihydrate, calcein-AM, ethidium homodimer-1, Triton X-100, Tween 20, bovine serum albumin (BSA), paraformaldehyde, fetal bovine serum (FBS), phosphate buffered saline, and ThermalSeal RTS Sealing Films were purchased from Sigma-Aldrich/Merck. Tyramine hydrochloride (99%) was purchased from Acros Organics. DMTMM was purchased from Fluorochem. Sodium alginate (80–120 cps) was purchased from FUJIFILM Wako Chemicals Europe. Rat tail collagen type I was purchased from Corning. Ruthenium and sodium persulfate were purchased from Advanced Biomatrix. Fluoresbryte YG microspheres (1.0 µm) were purchased from Polysciences. Polystyrene particles (50, 200, and 400 µm) were purchased from CD-Bioparticles and Sigma-Aldrich (150 µm). *N*-(2-hydroxyethyl)piperazine-29-(2-ethane-sulfonic acid) (HEPES), Dulbecco's modified Eagle's medium (DMEM), DMEM without phosphates, penicillin/streptomycin (pen/strep), Phalloidin-AF488, DAPI, trypsin–ethylenediaminetetraacetic acid, and BD Vacutainer Glass ACD Solution Tubes were purchased from Fisher Scientific/ThermoFisher. Recombinant Human Vascular Endothelial Growth Factor($VEGF_{165}$) was purchased from PeproTech. Water for cell culture (WFCC), endothelial cell growth basal medium-2 (EBM-2), and endothelial cell growth medium-2 Bullet kit (EGM-2) were purchased from Lonza. Sylgard 184 was obtained from Dow Corning. Anti-VE-Cadherin antibody (F-8) was purchased from Santa Cruz Biotechnology. Purified mouse anti-human ZO-1 was purchased from BD Biosciences. Goat anti-mouse immunoglobulins (IgG) H&L (Alexa Fluor 488) was purchased from Abcam. VACUETTE 9NC Coagulation Sodium Citrate 3.2% tubes were purchased from Geiner Bio-One. Heparin was obtained from LEO Pharma. Precision core nozzles were purchased from Subrex. Oxygen sensors spotted on ThermaSeal RTS Sealing Films were kindly provided by Stefanie Fuchs (TU Graz, Austria).

Material Synthesis: To synthesize alginate–tyramine, 1% w/v alginic acid sodium salt (80–120 cps) (1 g) was dissolved in MilliQ water (500 mL). Subsequently, 25 mM DMTMM and 25 mM Tyramine HCl were added and allowed to react for 24 h. Next, the solution was precipitated in ice-cold ethanol, filtered, and vacuum dried. The product was dialyzed against MilliQ water (Spectra/Por, molecular weight cut-off (MWCO) 1 kDa) for five days and finally lyophilized. To analyze the degree of substitution, UV–vis spectroscopy was used (NanoDrop ND-1000 spectrophotometer, 275 nm). The product typically contained ≈4.2 tyramine moieties per 100 repeating units.

Microgel Fabrication and Characterization: ATA microgels were produced by colliding a liquid microjet that contained 0.5% w/v ATA in H_2O with a second liquid microjet containing 0.1 M $CaCl_2$ and 10% EtOH v/v in H_2O at an angle of ≈40°. The first jet was actuated using a piezoelectric actuator to produce a stable droplet train. Microgels were collected in a solution containing 0.03 M $CaCl_2$ in H_2O. Microgels were typically produced at 0.9, 2.5, 3, and 4.5 mL min^{-1} flow rates using nozzles with an inner diameter of 50, 100, 150, and 250 µm, respectively. Flow rates were controlled using a neMESYS low-pressure syringe pump (Cetoni, Korbußen, Germany). For fluorescent visualization 0.1% w/v FITC-Dex 2000 kDa was added to the ATA containing precursor.

Microgels were visualized using fluorescence microscopy (EVOS FL Imaging System, ThermoFisher, Waltham, MA, USA) as well as confocal fluorescence microscopy using a Nikon A1 confocal microscope (Nikon, Tokyo, Japan). Size distributions and circularity measurements were performed using FIJI software.

Nanoindentation: The Young's modulus of ATA microgels was investigated using a nanoindenter (Pavone, Optics11 life). For the measurement, microgels were dispersed in MilliQ water and indented with a tip with 22.5 µm radius and a cantilever stiffness of 0.27 N m^{-1}. Each microgel was indented to a depth of 2 µm at a rate of 1 µm s^{-1}. The obtained load curves were fitted with a Hertzian fit. Fits with a $r^2 > 0.95$ were used for further processing.

Chip Fabrication: Microfluidic chip designs were created using computer-aided design (CAD) software (SolidWorks, Clewin). Silicon wafers were produced at the MESA+ Institute for Nanotechnology. Briefly, SU-8100 photoresist was spin-coated onto a silicon wafer with a final thickness of 250 µm. Following a baking step, the SU-8 layer was patterned by photolithography, after which it was baked again and developed according to the manufacturer's specifications. To produce polydimethylsiloxane (PDMS) chips, a PDMS prepolymer and curing agent (Sylgard 184) were mixed at a weight ratio of 10:1, poured onto the mold, and cured at 60 °C for 24 h. Inlets were punched using 1.5 mm punchers and the PDMS chips were bonded onto a glass slide using plasma treatment (Cute, Femto Science, Gyeonggi-do, South Korea).

PALM: To cross-link microgels using PALM, microgels were first pipetted into a 4 mm diameter mold with a height of 2 mm on a glass slide. The mold was packed with microgels by aspiration from below, resulting in a densely packed mass of microgels. Subsequently, the packed microgels were spiked with 1.25 mM ruthenium and 50 mM sodium persulfate solutions in H_2O and exposed to visible light for ≈3–5 min. The samples were subsequently removed and stored in H_2O for further use.

Nanoporous Gel Fabrication: Nanoporous ATA gels were prepared using ionic cross-linking by adding either an excess of 0.1 M $CaCl_2$ or a combination of 7.5 mM calcium carbonate and 30 mM glucono-δ-lactone (GDL) to 0.5% w/v ATA.

Pore Size Analysis (2D): PALM-generated ATA constructs were produced using microgels containing FITC-Dex 2000 kDa for fluorescent visualization. To analyze PALM-generated constructs, *Z*-stacks of ≈300 µm were obtained using confocal microscopy. Step size was 15 µm for PALM-generated constructs consisting of microgels produced with 50 and 100 µm nozzles and 33.5 µm for PALM-generated constructs consisting of microgels produced with 150 and 200 µm nozzles. For each condition, three samples were measured with an area of ≈2.35 × 2.35 mm per slice. For each sample, six slices were selected that were at least 100 µm deep into the sample to exclude the bottom edge of the sample from the analysis. Images were processed using a custom-built MATLAB script (Figure S7, Supporting Information) to calculate the area of individual pores. The equivalent diameter was obtained by converting the area to circles of equal area. Pores touching the edge of the image were excluded from analysis. All measured diameters for the pores were pooled per sample and averaged and binned per condition.

Micro-CT: Before micro-CT analysis, PALM-generated constructs were soaked overnight in a 3% w/v lead(II)acetate solution in H_2O. Afterward, PALM-generated constructs were transferred into a pipette tip containing H_2O for micro-CT analysis. Micro-CT imaging was performed on a Skyscan 2211 system (Bruker, Kontich, Belgium), equipped with a 11 MP charge-coupled device (CCD) camera. ATA samples were scanned with acquisition parameters set to 50 kV, 330 µA, rotation step of 0.47° over 360°, exposure time of 850 ms, and a frame averaging of 4 at a resolution of 1.5 µm voxel size for 150 µm diameter PALM-generated constructs and 0.65, 1.5, and 5 µm voxel size for 50, 150, and 200 µm diameter polystyrene spheres, respectively. For polystyrene samples, the source current was changed to 330 µA, the exposure time to 500 ms, and the rotation step to 0.23°, 0.43°/0.47°, and 0.43° over 360° for 50, 200, and 400 µm PS particles, respectively. Slice reconstruction was performed with NRecon

(v. 1.7.5, Bruker, Kontich, Belgium). For 3D visualization, Dragonfly software (v. 2021.1 Object Research Systems (ORS) Inc., Montreal, Canada, 2021) was used.

3D Analysis: To analyze the void fraction, micro-CT images were processed in CTAn (Bruker, Kontich, Belgium) and analyzed in 3D to obtain the void fraction. For each condition, three 1 mm^3 volumes were analyzed. Custom MATLAB scripts adapted from Rabbani et al.[57–59] were used to analyze 3D pore space, pore connectivity and to extract 3D visualizations of the pore networks. Micro-CT data were processed using CTAn to obtain binary thresholded images as input for the MATLAB scripts.

Flow Simulations: To estimate WSS in murine microvascular networks, Hagen–Poiseuille flow was solved for in a microvascular network with ≈70 000 vessel segments, extracted from the mouse brain cortex;[60] with a finite volume solver in DuMux 3.6[61,62] and pressure Dirichlet boundary conditions estimated[63] and provided in a published data set.[64] Both an apparent blood viscosity μ_{app} estimated by the nonlinear in vivo apparent viscosity relation proposed[49] (scaled to mouse red blood cells with volume 55 fL) and a constant value of $\mu_{app} = 3mPas$ were used. Only the former results were shown in Figure 2j as the difference in the WSS distribution was negligible. With the mass flow rate Q_{ij} in a cylindrical segment, its cross-sectional area A, and radius R, WSS ≈ $8\mu_{app}Q_{ij}/(AR)$. To estimate the wall shear stress distribution in ATA PALM-generated constructs, pore networks were extracted from three µ-CT images with resolution 666 px^3 at 1.5 μm^3 per pixel using PoreSpy 2.1[65] with Python 3.9.14 with PoreSpy's watershed algorithm in default setting. Single-phase fluid perfusion was simulated with a fixed pressure difference in three coordinate directions with closed side, top, and bottom boundaries using the pore-network solver of DuMux 3.6.[61,66] Transmissibilities t_{ij} were estimated with the method of Patzek and Silin[67] with shape factors for a circular cross-section[66] and a viscosity of $\mu = 3mPas$. The mass flow rate between two pores (i, j) with pressure p was computed by $Q_{ij} = t_{ij}\ (p_i - p_j)$ and WSS $\propto Q_{ij}/A^{3/2}$ for Newtonian fluids and fully developed laminar tube flow, where A was taken to be the throat (pore–pore interface) area computed by PoreSpy. For Figure 2j, the absolute WSS value (by scaling the pressure gradient applied across the sample) was scaled so that the average WSS over all pore–pore connections was equal to the average in the murine network (5.4 dyne cm^{-2}). Relative frequencies were computed as the number of pore–pore connections in each WSS bin divided by the total number of pore–pore connections in the sample. For annealed microgel samples, WSS distributions for each direction were averaged per sample.

Rheological Analysis: To analyze the effect of solvent on photoannealing, 8 mm hydrogel disks were formed using a silicone mold. Briefly, alginate–tyramine was dissolved at 1.5 w/v% along with 1.25 mM ruthenium and 20 mM sodium persulfate in either DMEM or MilliQ. Visible light was applied for 5 min to cross-link the hydrogels.

Rheological measurements were performed on a TA Instrument (Discovery series HR20). Hydrogel disks or PALM-generated annealed microgel constructs were placed in between a parallel plate configuration with 8 mm diameter. A constant initial axial force was maintained before each measurement, after which a frequency sweep was employed at room temperature within the viscoelastic regime at 1% strain from 1 to 10 $rads^{-1}$.

Hydraulic Conductivity Assay: A 4 mm diameter hole was drilled into the cap of a 15 mm polystyrene centrifuge tube, and a nylon membrane with 40 µm sized pores was glued onto the bottom of the cap. PALM-generated constructs and nanoporous gels were fabricated inside the hole. Afterward, the cap was attached to an inverted 15 mm polystyrene centrifuge tube with the tip sawed off. Then, a 10 mL water column was placed on top of the samples and water was collected into a collection tube below the sample for 10 min (PALM) or 15 h (nanoporous gels). Hydraulic conductivity was calculated based on Darcy's law

$$k = \frac{aL}{AT} \times \ln\left(\frac{W_2}{W_1}\right) \quad (1)$$

Here, a is the cross-section of the centrifuge tube, L is the sample thickness, A is the sample cross-sectional area, T is the measurement time, and W_2 and W_1 are the final and initial weight of the collection tube, representing the amount of water that passed through the sample.

Cell Culture: HepG2 human hepatocyte carcinoma cells were maintained in DMEM supplemented with 10% v/v FBS and 1% v/v pen/strep according to manufacturer's specifications. Cells were maintained at lower than 80% confluency.

HUVECs were maintained in EBM-2 supplemented with EGM-2 Bullet kit. Cells were maintained at lower than 80% confluency and used up until passage 5.

Cell Encapsulation: HepG2 cells were dissociated using trypsin and centrifuged down to remove medium. Cells were resuspended thoroughly in a 0.5% w/v ATA solution in H_2O containing 20 mM HEPES and 134 mM NaCl at pH 7.4 (HBS). After thorough resuspension, the cell suspension was passed over a 40 µm cell strainer to further dissociate cell clumps. The suspension was loaded into a 10 mL BD plastic syringe and connected to a neMESYS low pressure syringe pump (Cetoni, Korbußen, Germany). A second syringe containing 0.1 M $CaCl_2$ and 10% v/v EtOH in H_2O was connected to the pump with a 0.2 µm sterile filter in front. Microgels were produced as mentioned previously, typically with a 100 µm nozzle, and collected in a 0.03 M $CaCl_2$ solution in DMEM without phosphates.

After collection, cell-laden microgels were centrifuged gently (120 relative centrifugal force (RCF), 2 min) and resuspended in complete cell culture medium. Cell-laden microgels were cultured in 5% CO_2 and 37 °C. Cell viability was checked by removing 1 mL of cell-laden microgel suspension and incubating at room temperature with live/dead staining for 15 min according to the manufacturer's protocol.

To use PALM with cell-laden building blocks, cell-laden microgels were centrifuged gently and resuspended in DMEM without phosphates and pipetted into a 4 mm diameter mold. The packed microgels were then spiked with 1.25 mM ruthenium and 10 mM sodium persulfate. After cross-linking, engineered tissues were transferred into a bath of complete culture medium to wash out excess cross-linker solution, and finally placed in tissue culture plates and maintained at 5% CO_2 and 37 °C. To check for viability, engineered tissues were dissociated after cross-linking and incubated for 15 min with live/dead (calcein AM/ethidium-homodimer 1) staining according to the manufacturer's protocol.

To fix cell-laden PALM-generated tissues, they were gently washed with water for cell culture twice, followed by 1 h incubation in 4% w/v paraformaldehyde in H_2O containing 20 mM HEPES and 134 mM NaCl at pH 7.4. Samples were washed 2 more times with WFCC and stored at 4 °C.

Vascularization of Pore Space between Microgels: HUVECs were dissociated using trypsin and centrifuged down to remove medium. HUVECs were mixed with a 6 mg mL^{-1} rat tail collagen I solution at 600 000 cells mL^{-1} and mixed 1:1 with alginate beads. Solutions were then densely packed into microwells and allowed to cross-link for 30 min at 5% CO_2 and 37 °C, after which the top reservoir of the microwell was filled with EGM-2 medium supplemented with 50 ng mL^{-1} VEGF. Samples were cultured for seven days, and the medium was refreshed daily.

Immunofluorescence: PALM-generated tissues were permeabilized with 0.1% Triton X-100 for 30 min and incubated with 0.5 U mL^{-1} Phalloidin-AF488 for 1 h and 10 µg mL^{-2} DAPI for 20 min.

Vascularized constructs were permeabilized for 10 min with 0.3% v/v Triton X-100 and subsequently blocked overnight with a blocking buffer containing 3% w/v BSA, 0.3% v/v Triton X-100, and 0.1% v/v Tween 20 followed by overnight incubation with the primary antibody (VE-Cadherin or tight junction protein 1 (ZO-1), 1:200 dilution). The next day, samples were washed 3 times 0.3% v/v Triton X-100 followed by overnight incubation with the secondary antibody (Goat-Anti Mouse 488, Donkey-Anti Mouse 647, 1:200 dilution). Finally, samples were incubated with DAPI (1:100) for 20 min and washed twice more prior to imaging.

Whole Blood Isolation and Staining: Human whole blood was collected from anonymous healthy volunteers by the TechMed Blood Donor Service from the Technical Medical Centre, University of Twente. Fresh venous human blood (8.5 mL) was collected in BD Vacutainer Glass ACD Solution Tubes and used within 4 h of withdrawal. The research did not fall in the scope of the Dutch Medical Research Involving Human Subjects Act. In agreement with the Declaration of Helsinki, informed consent

was obtained from all volunteers. Furthermore, the blood collection procedure was approved by the local medical research ethics committee (METC Twente). To stain cells, $DiOC_6$ was added to a final concentration of 0.5 µg mL^{-1} and incubated for 10 min. Prior to perfusion with whole blood, microfluidic chips were washed using a wash buffer containing 1 M HEPES, 1% w/v BSA, 1% w/v glucose, 200 mM $CaCl_2$, and 1 U mL^{-1} heparin. To perfuse PALM-generated constructs, a pipette tip was filled with RBC solution and placed on the inlet of the previously described microfluidic chip.

Red Blood Cell Isolation and Staining: For RBC isolation, fresh venous human blood was collected in VACUETTE 9NC Coagulation sodium citrate 3.2% tubes. Blood was centrifuged at 500 g for 2 min and the plasma and buffy coat were removed. The removed volume was replaced by HBS and erythrocytes were centrifuged and washed with HBS thrice more. Finally, the resulting suspension of red blood cells was diluted 50 times (low concentration) or 10 times (high concentration) in HBS. To perfuse PALM-generated constructs, a pipette tip was filled with RBC solution and placed on the inlet of the previously described microfluidic chip.

Perfusion of Constructs Generated through PALM: For perfusion experiments, microgels were loaded into a PDMS chip containing pillar traps. After packing microgels into the chip, ruthenium and sodium persulfate solutions were mixed 1:1 and injected into the chip. Chips were then exposed to visible light for ≈3–5 min. After cross-linking, chips were gently flushed with H_2O to wash out the residual cross-linker.

To visualize pore interconnectivity, a solution containing 0.1% w/v fluoresbrite green fluorescent microspheres was perfused into the PALM-generated constructs using a syringe pump (Harvard Apparatus, PHD Ultra) at a flow rate of 10 µL h^{-1}. Images were captured using an inverted microscope (IX51, Olympus, Japan) equipped with a high-speed camera (ORCA-Flash 4.0 LT, Hamamatsu Photonics, Japan).

Two reservoirs containing H_2O and a 0.1 mg mL^{-1} Rhodamine B solution in H_2O were connected to the two outlets to analyze small molecule diffusivity. To flow solutions in the direction of the sample, 10 mbar of pressure was applied to the reservoir of choice. A pressure control unit (MFCS-EZ, Fluigent, France) and a 2-way microfluidic valve (2-switch, Fluigent, France) were used to control the flow of liquids and rapidly switch between the two liquids. Fluorescent images were captured using an inverted microscope (IX51, Olympus, Japan) equipped with a high-speed camera (ORCA-Flash 4.0 LT, Hamamatsu Photonics, Japan).

Nanoporous hydrogels were produced on-chip by injecting a solution containing 7.5 mM $CaCO_3$, 30 mM GDL, and 0.5% w/v alginate into a microfluidic chamber after mixing and allowing it to cross-link.

Small molecule diffusivity in nanoporous hydrogels within the chip was analyzed by filling the reservoirs of the chip with a total of 200 µL of 0.1 mg mL^{-1} Rhodamine B solution in H_2O and imaged using an inverted microscope (IX51, Olympus, Japan) equipped with a high-speed camera (ORCA-Flash 4.0 LT, Hamamatsu Photonics, Japan).

Oxygen Measurements: For oxygen measurements, poly(methyl methacrylate) (PMMA) chips were fabricated using a Computer Numerical Control micromilling machine (Datron Neo, Mühltal, Germany). Optical sensors that were spotted onto ThermalSeal RTS Sealing Films similar to the method described by Fuchs et al.[68] were obtained from Graz University of Technology. Oxygen sensor films were used to seal the bottom of the microfluidic PMMA chip. The sensors were placed ≈6 mm from the side channel. PALM-generated or nanoporous hydrogels were cross-linked in the microfluidic chip as described under perfusion of constructs generated through PALM. Optical fibers were fixed underneath the oxygen sensor spots and connected to a phasefluorimeter (Firesting Pro, PyroScience GmbH, Germany). Before use, sensors were calibrated using a two-point calibration at ambient air and under N_2 flow to achieve a 0% oxygen calibration point. Calibration and measurements were performed at room temperature.

To measure changes in oxygen tension, chips were first degassed at 0.1% oxygen for 30 min in an Xvivo System Model X3 Cytocentric Cell Incubation and Handling Platform (BioSpherix, Ltd., USA). Subsequently, MilliQ was perfused into the side channel of the chip and allowed to diffuse (nanoporous hydrogels) or applied with convective force (PALM). Samples were measured until a plateau was reached (i.e., saturation). For each condition, three separate samples were measured and averaged. Data were normalized to both the starting and end (plateau) value to be able to compare the differences in oxygen influx between conditions.

Statistics and Figures: All statistical analysis was performed in OriginPro 2019b. Significance was determined using one-way analysis of variance (ANOVA) tests and post hoc Tukey's test. Significance of $p < 0.05$ and $p < 0.001$ were indicated by * and ***, respectively. Nonsignificant difference area was indicated by n.s. All graphs were created using OriginPro 2019b, schematics were created using Adobe Illustrator. 3D reconstructions were generated using FIJI, Dragonfly, Imaris, and MATLAB R2020a.

Supporting Information

Supporting Information is available from the Wiley Online Library or from the author.

Acknowledgements

The authors thank Stefanie Fuchs (TU Graz, Austria) for providing oxygen sensors. The authors thank the TechMed Donor Service of the University of Twente and respective donors. J.L. acknowledges financial support from the Dutch Research Council (Vidi, Grant No. 17522) and the European Research Council (Starting Grant, No. 759425). T.K. acknowledges financial support from the European Union's Horizon 2020 Research and Innovation programme under the Marie Skłodowska-Curie Actions Grant Agreement No. 801133.

Conflict of Interest

The authors declare no conflict of interest.

Data Availability Statement

The data that support the findings of this study are available from the corresponding author upon reasonable request.

Keywords

biofabrication, microfluidics, perfusion, tissue engineering, vascularization

Received: September 1, 2023
Revised: November 21, 2023
Published online:

[1] M. A. Traore, S. C. George, *Tissue Eng., Part B* **2017**, *23*, 505.
[2] J. Rouwkema, A. Khademhosseini, *Trends Biotechnol.* **2016**, *34*, 733.
[3] R. K. Jain, P. Au, J. Tam, D. G. Duda, D. Fukumura, *Nat. Biotechnol.* **2005**, *23*, 821.
[4] R. J. Mcmurtrey, *Tissue Eng., Part C* **2016**, *22*, 221.
[5] X. Meng, Y. Xing, J. Li, C. Deng, Y. Li, X. Ren, D. Zhang, *Front. Cell Dev. Biol.* **2021**, *9*, 639299.
[6] J. Rouwkema, B. F. J. M. Koopman, C. A. V. Blitterswijk, W. J. A. Dhert, J. Malda, *Biotechnol. Genet. Eng. Rev.* **2009**, *26*, 163.
[7] S. Kim, H. Lee, M. Chung, N. L. Jeon, *Lab Chip* **2013**, *13*, 1489.
[8] S. W. Chen, A. Blazeski, S. Zhang, S. E. Shelton, G. S. Offeddu, R. D. Kamm, *Lab Chip* **2023**, *23*, 4552.
[9] M. Nakamura, Y. Ninomiya, K. Nishikata, N. Futai, *Jpn. J. Appl. Phys.* **2022**, *61*, SD1040.

[10] N. Awad, H. Niu, U. Ali, Y. Morsi, T. Lin, *Membranes* **2018**, *8*, 15.
[11] F. Helms, S. Lau, T. Aper, S. Zippusch, M. Klingenberg, A. Haverich, M. Wilhelmi, U. Böer, *Ann. Biomed. Eng.* **2021**, *49*, 2066.
[12] S. Zhang, M. Zhou, Z. Ye, Y. Zhou, W.-S. Tan, *Biotechnol. J.* **2017**, *12*, 1700008.
[13] P. Dhakane, V. S. Tadimarri, S. Sankaran, *Adv. Funct. Mater.* **2022**, *33*, 2212695.
[14] T. Limongi, L. Brigo, L. Tirinato, F. Pagliari, A. Gandin, P. Contessotto, A. Giugni, G. Brusatin, *Biomed. Mater.* **2021**, *16*, 035013.
[15] A. A. Szklanny, M. Machour, I. Redenski, V. Chochola, I. Goldfracht, B. Kaplan, M. Epshtein, H. Simaan Yameen, U. Merdler, A. Feinberg, D. Seliktar, N. Korin, J. Jaros, S. Levenberg, *Adv. Mater.* **2021**, *33*, 2102661.
[16] P. Gutowski, S. M. Gage, M. Guziewicz, M. Ilzecki, A. Kazimierczak, R. D. Kirkton, L. E. Niklason, A. Pilgrim, H. L. Prichard, S. Przywara, R. Samad, B. Tente, J. Turek, W. Witkiewicz, N. Zapotoczny, T. Zubilewicz, J. H. Lawson, *J. Vasc. Surg.* **2020**, *72*, 1247.
[17] S. Y. Hann, H. Cui, G. Chen, M. Boehm, T. Esworthy, L. G. Zhang, *Biomed. Eng. Adv.* **2022**, *4*, 100065.
[18] R. D. Kirkton, M. Santiago-Maysonet, J. H. Lawson, W. E. Tente, S. L. M. Dahl, L. E. Niklason, H. L. Prichard, *Sci. Transl. Med.* **2019**, *11*, eaau6934.
[19] D. B. Kolesky, K. A. Homan, M. A. Skylar-Scott, J. A. Lewis, *Proc. Natl. Acad. Sci. USA* **2016**, *113*, 3179.
[20] A. Lee, A. R. Hudson, D. J. Shiwarski, J. W. Tashman, T. J. Hinton, S. Yerneni, J. M. Bliley, P. G. Campbell, A. W. Feinberg, *Science* **2019**, *365*, 482.
[21] I. Orellano, A. Thomas, A. Herrera, E. Brauer, D. Wulsten, A. Petersen, L. Kloke, G. N. Duda, *Adv. Funct. Mater.* **2022**, *32*, 2208325.
[22] E. P. Chen, Z. Toksoy, B. A. Davis, J. P. Geibel, *Front. Bioeng. Biotechnol.* **2021**, *9*, 664188.
[23] W. Wu, A. DeConinck, J. A. Lewis, *Adv. Mater.* **2011**, *23*, H178.
[24] M. A. Skylar-Scott, S. G. M. Uzel, L. L. Nam, J. H. Ahrens, R. L. Truby, S. Damaraju, J. A. Lewis, *Sci. Adv.* **2019**, *5*, eaaw2459.
[25] J. Kajtez, M. F. Wesseler, M. Birtele, F. R. Khorasgani, D. Rylander Ottosson, A. Heiskanen, T. Kamperman, J. Leijten, A. Martínez-Serrano, N. B. Larsen, T. E. Angelini, M. Parmar, J. U. Lind, J. Emnéus, *Adv. Sci.* **2022**, *9*, 2201392.
[26] X. Cao, S. Maharjan, R. Ashfaq, J. Shin, Y. S. Zhang, *Engineering* **2021**, *7*, 832.
[27] M. A. Biederman-Thorson, R. F. Schmidt, G. Thews, *Human Physiology*, Springer, Singapore, **2013**.
[28] J. M. De Rutte, J. Koh, D. Di Carlo, *Adv. Funct. Mater.* **2019**, *29*, 1900071.
[29] D. R. Griffin, W. M. Weaver, P. O. Scumpia, D. Di Carlo, T. Segura, *Nat. Mater.* **2015**, *14*, 737.
[30] N. J. Darling, E. Sideris, N. Hamada, S. T. Carmichael, T. Segura, *Adv. Sci.* **2018**, *5*, 1801046.
[31] R.-S. Hsu, P.-Y. Chen, J.-H. Fang, Y.-Y. Chen, C.-W. Chang, Y.-J. Lu, S.-H. Hu, *Adv. Sci.* **2019**, *6*, 1900520.
[32] J. Koh, D. R. Griffin, M. M. Archang, A.-C. Feng, T. Horn, M. Margolis, D. Zalazar, T. Segura, P. O. Scumpia, D. Di Carlo, *Small* **2019**, *15*, 1903147.
[33] A. R. Anderson, E. Nicklow, T. Segura, *Acta Biomater.* **2022**, *150*, 111.
[34] T. H. Qazi, J. Wu, V. G. Muir, S. Weintraub, S. E. Gullbrand, D. Lee, D. Issadore, J. A. Burdick, *Adv. Mater.* **2022**, *34*, 2109194.
[35] A. C. Suturin, A. J. D. Krüger, K. Neidig, N. Klos, N. Dolfen, M. Bund, T. Gronemann, R. Sebers, A. Manukanc, G. Yazdani, Y. Kittel, D. Rommel, T. Haraszti, J. Köhler, L. De Laporte, *Adv. Healthcare Mater.* **2022**, *11*, 2200989.
[36] D. Ribezzi, M. Gueye, S. Florczak, F. Dusi, D. de Vos, F. Manente, A. Hierholzer, M. Fussenegger, M. Caiazzo, T. Blunk, J. Malda, R. Levato, *Adv. Mater.* **2023**, *35*, 2301673.
[37] H. E. White, S. F. Walton, *J. Am. Ceram. Soc.* **1937**, *20*, 155.
[38] M. Alonso, E. Sainz, F. Lopez, K. Shinohara, *Chem. Eng. Sci.* **1995**, *50*, 1983.
[39] C. W. Visser, T. Kamperman, L. P. Karbaat, D. Lohse, M. Karperien, *Sci. Adv.* **2018**, *4*, eaao1175.
[40] J. Jiang, G. Shea, P. Rastogi, T. Kamperman, C. H. Venner, C. W. Visser, *Adv. Mater.* **2021**, *33*, 2006336.
[41] B. van Loo, S. A. ten Den, N. Araújo-Gomes, V. de Jong, R. R. Snabel, M. Schot, J. M. Rivera-Arbeláez, G. J. C. Veenstra, R. Passier, T. Kamperman, J. Leijten, *Nat. Commun.* **2023**, *14*, 6685.
[42] B. van Loo, S. S. Salehi, S. Henke, A. Shamloo, T. Kamperman, M. Karperien, J. Leijten, *Mater. Today Bio* **2020**, *6*, 100047.
[43] A. Pellé, M. Durand, *arXiv preprint arXiv:2302.11901* **2023**.
[44] A. Saint-Jalmes, *Soft Matter* **2006**, *2*, 836.
[45] G. D. Scott, D. M. Kilgour, *J. Phys. D: Appl. Phys.* **1969**, *2*, 863.
[46] J. H. Conway, N. J. A. Sloane, *Sphere Packings, Lattices and Groups*, Springer, Singapore, **2013**.
[47] M. M. Roozbahani, L. Graham-Brady, J. D. Frost, *Int. J. Numer. Anal. Methods Geomech.* **2014**, *38*, 1776.
[48] M. Roozbahani, R. Borela, J. Frost, *Materials* **2017**, *10*, 1237.
[49] A. R. Pries, T. W. Secomb, *Am. J. Physiol.: Heart Circ. Physiol.* **2005**, *289*, H2657.
[50] F. Schmid, M. J. P. Barrett, D. Obrist, B. Weber, P. Jenny, *PLoS Comput. Biol.* **2019**, *15*, 1007231.
[51] A. G. Koutsiaris, S. V. Tachmitzi, N. Batis, M. G. Kotoula, C. H. Karabatsas, E. Tsironi, D. Z. Chatzoulis, *Biorheology* **2007**, *44*, 375.
[52] Y. Huo, C. O. Linares, G. S. Kassab, *Circ. Res.* **2007**, *100*, 273.
[53] M. I. Neves, L. Moroni, C. C. Barrias, *Front. Bioeng. Biotechnol.* **2020**, *8*, 665.
[54] G. Ramirez-Calderon, H. H. Susapto, C. A. Hauser, *ACS Appl. Mater. Interfaces* **2021**, *13*, 29281.
[55] C. K. Griffith, C. Miller, R. C. A. Sainson, J. W. Calvert, N. L. Jeon, C. C. W. Hughes, S. C. George, *Tissue Eng.* **2005**, *11*, 257.
[56] W. Sekine, Y. Haraguchi, T. Shimizu, A. Umezawa, T. Okano, *J. Biochips Tissue Chips* **2011**, *1*, 2153.
[57] A. Rabbani, M. Babaei, *Adv. Water Resour.* **2019**, *126*, 116.
[58] A. Rabbani, S. Ayatollahi, R. Kharrat, N. Dashti, *Adv. Water Resour.* **2016**, *94*, 264.
[59] A. Rabbani, S. Jamshidi, S. Salehi, *J. Pet. Sci. Eng.* **2014**, *123*, 164.
[60] P. Blinder, P. S. Tsai, J. P. Kaufhold, P. M. Knutsen, H. Suhl, D. Kleinfeld, *Nat. Neurosci.* **2013**, *16*, 889.
[61] T. Koch, D. Gläser, K. Weishaupt, S. Ackermann, M. Beck, B. Becker, S. Burbulla, H. Class, E. Coltman, S. Emmert, T. Fetzer, C. Grüninger, K. Heck, J. Hommel, T. Kurz, M. Lipp, F. Mohammadi, S. Scherrer, M. Schneider, G. Seitz, L. Stadler, M. Utz, F. Weinhardt, B. Flemisch, *Comput. Math. Appl.* **2021**, *81*, 423.
[62] O. Sander, T. Koch, N. Schröder, B. Flemisch, *Arch. Numer. Software* **2017**, *5*, 217.
[63] F. Schmid, P. S. Tsai, D. Kleinfeld, P. Jenny, B. Weber, *PLoS Comput. Biol.* **2017**, *13*, 1005392.
[64] F. Schmid, P. Jenny, B. Weber, D. Kleinfeld, [Data set] Zenodo, **2017**, https://doi.org/10.5281/zenodo.758632.
[65] J. Gostick, Z. Khan, T. Tranter, M. Kok, M. Agnaou, M. Sadeghi, R. Jervis, *J. Open Source Software* **2019**, *4*, 1296.
[66] K. Weishaupt, T. Koch, R. Helmig, *Drying Technol.* **2022**, *40*, 697.
[67] T. W. Patzek, D. B. Silin, *J. Colloid Interface Sci.* **2001**, *236*, 295.
[68] S. Fuchs, V. Rieger, A. Ø. Tjell, S. Spitz, K. Brandauer, R. Schaller-Ammann, J. Feiel, P. Ertl, I. Klimant, T. Mayr, *Biosens. Bioelectron.* **2023**, *7*, 115491.